Lattice-Boltzmann modeling of buoyancy-driven turbulent flows

Mostafa Taha, Song Zhao, Aymeric Lamorlette, Jean-Louis Consalvi, Pierre Boivin

Lattice-Boltzmann modeling of buoyancy-driven turbulent flows

M. Taha,[1] S. Zhao 赵崧),[1] A. Lamorlette,[2] J.L. Consalvi,[2] and P. Boivin[1, a)]

[1)] *Aix Marseille Univ, CNRS, Centrale Marseille, M2P2, Marseille, France*

[2)] *Aix Marseille Univ, CNRS, IUSTI, Marseille, France*

(Dated: May 8, 2022)

The pressure-based hybrid lattice-Boltzmann method presented by Farag & al in Phys. Fluids, vol. 32, p. 066106 (2020) is assessed for the simulation of buoyancy driven flows. The model is first validated on Rayleigh-Benard and Rayleigh-Taylor two-dimensional cases. A large-eddy simulation of a turbulent forced plume is then carried out, and results are validated against experiments. A good overall agreement is obtained, both for mean and fluctuations quantities, as well as global entrainment. The self-similarity characteristic of the plume in the far-field is also recovered.

[a)]Electronic mail: pierre.boivin@univ-amu.fr

INTRODUCTION

Lattice Boltzmann Methods (LBM) are a powerful tool for the simulation of fluid dynamics[1]. Due to its attractive computational cost[2], its capacities for massively parallel computing and the ease to deal with complex geometries using multi-level Cartesian grids, these methods have attracted growing interest both in the academic and industrial spheres in the past decade[3–5].

LBM being initially designed to tackle isothermal flows, extension to thermal flows is today an active topic of investigation in the community. In achieving that goal, the numerical stability of the collision operator, at the heart of the method, used to be a major issue. The single relaxation time Bhatnagar-Gross-Krook model[6], probably the most popular model, lacks stability for shear flows, but more recent models such as multiple relaxation collision[7] or regularized kernels[8,9] significantly improved stability. Another issue is the resolution of energy or temperature equation, which cannot be straightforwardly achieved on low-order lattices[5]. Two main options are available in the literature. The first is the double distribution function (DDF) option that consists in coupling the LBM solver with a second distribution function, whose main order corresponds to either temperature, energy, or enthalpy (see, e.g.[10,11], for recent studies). A second option is to couple directly LBM with a scalar (temperature, energy, enthalpy), solved in a coupled finite difference solver. This second option was found attractive, as it allows, for a reasonable cost[2], to include an arbitrary number of additional scalar equations. Following recent successful applications to compressible[12–17], atmospheric[18–22] or reactive flows[23–25], the second option, often referred to as hybrid LBM is retained for this study. This works aims at investigating their applicability to buoyancy driven flows, such as those encountered in fire-related problems[26].

The far field of turbulent, axisymmetric, free-plume in a quiescent, unstratified environment, where buoyancy-driven plume exhibits self-similar behavior, play a significant role in various fluid flows of environmental and technological importance, including thermal plumes that arise due to the convective heating on Earth's surface[27–29], fire protection engineering with problems associated with fire detection, smoke filling rates of indoor spaces, fire venting, fire heating of structural elements of buildings[30], wildland fires[31,32], dispersal of volcanic eruptions[33–35], sea ice plumes[36,37], smoke stacks[38], and cooling tower plume dispersion[39]. Forced plumes or buoyant jets represent a canonical configuration to study such plumes.

They consist by releasing the plumes from a source with some initial momentum. The flow can be decomposed into three regions: (i) a region featuring a jet-like behavior near the source, (ii) a transitional region and (iii) further downstream, the far-field fully-developed buoyancy-driven plume[40].

The first far-field plume theories[41–43] assumed a turbulent flow, a point source of buoyancy, the Boussinesq approximation and a dynamic similarity of the mean and turbulent motion at all elevations. Morton at al.[43] developed an integral formulation by assuming both "top-hat" radial profiles for both velocity and temperature (density) and a point source, and by introducing an entrainment coefficient, α, defined as the ratio of radial velocity at the edge of the plume to the vertical velocity within the plume. Their model predicts correctly the scaling laws for the plume radius, that increases linearly with height, z, as well as for both velocity and temperature rise above the ambient that decay as $z^{-1/3}$ and $z^{-5/3}$, respectively. The weak plume formulation of Morton et al.[43] was extended to "strong plumes" by removing both the Boussinesq approximation and the point source assumption through the introduction of a virtual origin and, by considering more realistic Gaussian profiles for both velocity and temperature[30]. This in conjunction with experiments in fire plumes above the flames[44] provided expressions for plume radius and centreline velocity and temperature consistent with experimental data[45–47]. Another important feature of buoyant plumes is that the radial profiles of dimensionless mean velocity and temperature and dimensionless rms turbulent fluctuations of velocity and temperature exhibit a self-similar behaviour with $\eta = r/z$ as a self-similar variable, where r is the radial coordinate[45–49]. Progress was also made in the understanding of the role of buoyancy on the entrainment process and the flow behavior. In particular, Saeed et al. found that buoyancy contributes to enhance the mean kinetic energy budget but also the momentum flux[50].

The CFD modeling of forced plumes was also a very active research area. A significant amount of Reynolds-Averaged Navier-Stokes simulations were reported with different formulations of the k-ϵ model[51–54]. On the other hand, Zhou et al.[55] and Yan[56] showed the capability of Large Eddy Simulation (LES) to predict well the plume's puffing, self-preserving and spreading. LES of forced jet were also performed[57] to evaluate the energy-consistent approach for modeling entrainment rate coefficient, α, developed by Kaminski et al.[58] and van Reeuwijk and Craske[59]. Direct numerical simulation (DNS) and LES of thermal plumes were also reported[60–63]. These studies focused mainly on the generation and growth of

buoyancy-induced instabilities in the near field that governs the transition from laminar to turbulence. In particular, it was shown that these instabilities have to be fully resolved to capture the dynamics of such purely buoyant thermal plumes[60]. In addition, the DNS was found in good agreement with experimental data in the far field[61].

This literature survey reveals that all the numerical investigations were performed by using a low Mach-formulation of the Navier-Stokes equation. To the authors' best knowledge, no attempt to consider lattice-Boltzmann method was reported.

The goal in the current work is to assess the ability of the pressure-based Lattice-Boltzmann method proposed by Farag et al.[16] to correctly predict the behavior of a forced plume in the self-similarity region away from the source. This manuscript is organized as follows. The first Section recalls the target macroscopic equations, as well as the Lattice-Boltzmann algorithm proposed. The second Section presents a number of 2D canonical flow validations, including Rayleigh-Benard and Rayleigh-Taylor instabilities. The third Section presents a large eddy simulation of the plume experimentally described by Shabbir and George[47], along with comparisons with the large eddy simulation presented by Zhou et al.[55] and the theoretical model of Morton[28,43]. All the simulations were performed using the compressible ProLB code[64].

I. LATTICE-BOLTZMANN MODEL FOR COMPRESSIBLE FLOWS

A. Macroscopic governing equations

The flow mass, momentum and energy conservation equations are introduced as:

$$\frac{\partial \rho}{\partial t} + \frac{\partial \rho u_i}{\partial x_i} = 0 \tag{1}$$

$$\frac{\partial \rho u_i}{\partial t} + \frac{\partial \rho u_i u_j + \delta_{ij} p}{\partial x_j} = \frac{\partial \Pi_{ij}}{\partial x_j} + \rho g_i, \qquad (i = 1, 2, 3) \tag{2}$$

$$\rho \frac{\partial h}{\partial t} + \rho u_j \frac{\partial h}{\partial x_j} = \frac{Dp}{Dt} - \frac{\partial q_j}{\partial x_j} + \Pi_{ij} \frac{\partial u_i}{\partial x_j}, \tag{3}$$

where ρ is the mass volume, u_i is the velocity vector, p is the pressure, g_i is the gravitational acceleration, h is the mass enthalpy and δ_{ij} as the Kronecker delta symbol. Throughout this manuscript, we neglect the pressure work $\frac{Dp}{Dt} = \frac{\partial p}{\partial t} + u_j \frac{\partial p}{\partial x_j} \approx 0$ in the energy equation, a reasonable approximation for buoyancy driven flows. The stress tensor Π_{ij} in Eqs. (2-3)

reads

$$\Pi_{ij} = \mu \left(\frac{\partial u_i}{\partial x_j} + \frac{\partial u_j}{\partial x_i} - \delta_{ij} \frac{2}{3} \frac{\partial u_k}{\partial x_k} \right), \tag{4}$$

with μ the dynamic viscosity. Finally, the heat flux q_i in the energy equation reads

$$q_i = -\lambda \frac{\partial T}{\partial x_i} \tag{5}$$

where T is the temperature, and λ the heat conductivity, obtained assuming constant Prandtl number:

$$\mathrm{Pr} = \frac{c_p \mu}{\lambda} = \frac{\nu}{\alpha}, \tag{6}$$

where ν is the kinematic viscosity defined as $\nu = \mu/\rho$ while α is the thermal diffusivity defined as $\alpha = \lambda/\rho c_p$. The system of Eqs (1-3) is fully closed by the choice of an equation of state

$$p = \rho.r.T, \qquad h = c_p.T, \tag{7}$$

with c_p the mass heat capacity at constant pressure, and $r = 287 \mathrm{J\,kg^{-1}\,K^{-1}}$ is the gas constant for air per unit mass. Note that we assume c_p to be constant, since the temperature in the test cases presented does not exceed 600K.

B. Turbulence modeling

For the large eddy simulation presented in Sec. III, a Vreman eddy-viscosity subgrid scale model is used[65]. The filtered expressions for Eqs. (1-3) are widely reported in the literature (see, e.g.[66]) and not recalled here. Applying the subgrid-scale model numerically comes down to modifying the viscosity μ through the addition of a turbulent viscosity μ_t obtained as:

$$\mu_t = \rho C \sqrt{\frac{B_\beta}{\alpha_{ij}\alpha_{ij}}}, \tag{8}$$

with

$$\alpha_{ij} = \frac{\partial u_j}{\partial x_i}, \tag{9}$$

$$\beta_{ij} = \Delta_m^2 \alpha_{mi} \alpha_{mj}, \tag{10}$$

$$B_\beta = \beta_{11}\beta_{22} - \beta_{12}^2 + \beta_{11}\beta_{33} - \beta_{13}^2 + \beta_{22}\beta_{33} - \beta_{23}^2, \tag{11}$$

The constant C is related to the Smagorinsky constant C_s as $C = 2.5 C_s^2$. Δ_m is the local mesh size. The model is simple to implement and compute as it only requires the

local filter width (i.e. mesh size) and the first order derivatives of the velocity field. In our simulation $C_s = 0.1$, following Vreman's recommendation[65], which was also adopted in the forced plume large eddy simulation by Zhou et al.[55]. The heat flux takes into account the subgrid contribution via a turbulent Prandtl number Pr_t.

C. Numerical method: Lattice Boltzmann solver

For a complete description of the numerical method, the reader is referred to Farag et al.[16,17]. Lattice-Boltzmann methods are derived from a space, time and velocity discretization of the Boltzmann equation[5]. In the present model, the probability density function f_i is solved at each point x via the Boltzmann equation discretized as:

$$f_i\left(x + c_i\delta t, t + \delta t\right) = f_i^{\mathrm{eq}}\left(x,t\right) + \left(1 - \frac{\delta t}{\tau}\right) f_i^{\mathrm{neq}}\left(x,t\right) + \frac{\delta t}{2} F_i^E(x,t) \tag{12}$$

where δt is the time-step, and c_i is the i^{th} discrete velocity of the D3Q19 lattice[67], and F_i^E is a volume force including gravity and correcting terms, as defined in Appendix A. The equilibrium and off-equilibrium populations ($f_i^{\mathrm{eq}}, f_i^{\mathrm{neq}}$) are to be defined in Eqs (14, 16).

In Eq. (12), the relaxation time τ is related to the dynamic viscosity as:

$$\tau = \frac{\mu}{\rho c_s^2} + \frac{\delta_t}{2}, \tag{13}$$

where $c_s = \delta x/(\sqrt{3}\delta t)$ is the characteristic velocity of the D3Q19 lattice[67].

The equilibrium function is obtained as:

$$f_i^{\mathrm{eq}} = \omega_i \left(\rho\theta + \frac{\mathcal{H}_{i,\alpha}^{(1)}}{c_s^2}\rho u_\alpha + \frac{\mathcal{H}_{i,\alpha\beta}^{(2)}}{2c_s^4}\rho u_\alpha u_\beta + a^{(3)} + a^{(4)} \right), \tag{14}$$

where ω_i is the D3Q19 weight of discrete velocity c_i, $\mathcal{H}_i$ are the discrete Hermite polynomials, defined in Appendix A, and $a^{(3)}$ and $a^{(4)}$ are third and forth order terms also provided in Appendix A. The reduced temperature θ reads

$$\theta = \frac{rT}{c_s^2}. \tag{15}$$

The off-equilibrium counterpart f^{neq} is obtained as:

$$f_i^{\mathrm{neq}} = \omega_i \left[\frac{\mathcal{H}_{i,\alpha\beta}^{(2)}}{2c_s^4} a_{\alpha\beta}^{(2),\mathrm{neq}} + \frac{\mathcal{H}_{i,\gamma}^{(3r)}}{6c_s^6} a_{\gamma}^{(3r),\mathrm{neq}} \right], \tag{16}$$

with

$$a_{\alpha\beta}^{(2),\mathrm{neq}} \equiv a_{\alpha\beta}^{*(2),\mathrm{neq}} - \frac{\delta_{\alpha\beta}}{3} a_{\gamma\gamma}^{*(2),\mathrm{neq}}, \tag{17}$$

$$a_{\alpha\beta}^{*(2),\mathrm{neq}} = \sum_i \left[\left(f_i - f_i^{\mathrm{eq}} + \frac{\delta t}{2} F_i^E \right) \mathcal{H}_{i,\alpha\beta}^{(2)} \right]. \tag{18}$$

and the third-order contribution defined in Appendix A.

Finally, the macroscopic variables are reconstructed from f_i as:

$$\rho(t+\delta_t, x) = \sum_i f_i(t+\delta_t, x) - (\rho\theta)(t,x) + \rho(t,x) \tag{19}$$

$$\rho u_i(t+\delta_t, x) = \sum_i c_i \left(f_i(t+\delta_t, x) + \frac{\delta_t}{2} F_i^g \right). \tag{20}$$

where F_i^g is the gravity force term defined in Appendix A. The enthalpy equation (3) is solved at the same time using a finite difference discretization under non-conservative form, exactly as presented by Tayyab *et al.*[23,24]. Second-order consistency to the macroscopic equations (1-3) can be shown via Chapman-Enskog[5], or Taylor[68,69] expansions.

II. CANONICAL 2D VALIDATIONS

This Section provides canonical validations of the numerical method presented above. It focuses on two gravity-driven configurations: the Rayleigh-Benard and Rayleigh-Taylor instabilities, since the properties of the flow solver are already validated in a large number of compressible flow configurations in the absence of gravity[2,16,17,19,24,25,70].

A. Rayleigh-Benard Instability

The Rayleigh-Benard instability is a configuration involving natural convection and heat transfer[71].

Figure 1 depicts the configuration to be simulated. It consists of a square box of dimension $1\,\mathrm{m} \times 1\,\mathrm{m}$ initially filled with quiescent air, and surrounded by adiabatic walls on the left and right, and isothermal top and bottom walls, resp. at $T_C = 299.5\mathrm{K}$ and $T_H = 300.5\mathrm{K}$.

The Rayleigh number, Ra, describes, on the one hand, the balance between buoyancy versus viscous forces in the momentum equation and, on the other hand, the balance between

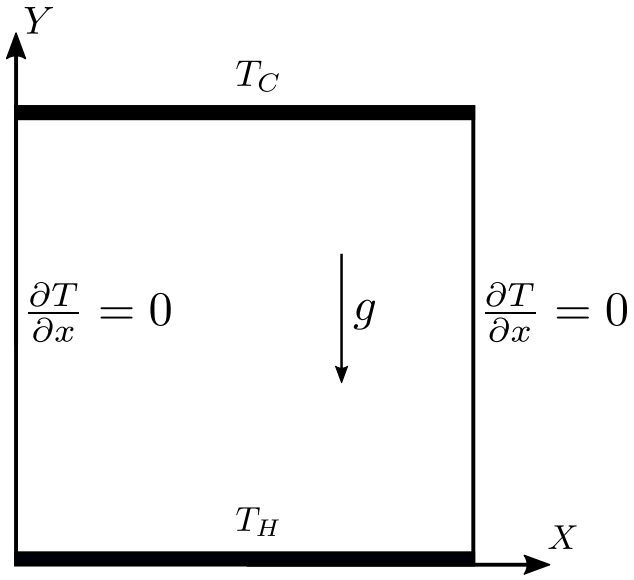

Figure 1: Schematic of Rayleigh Benard test case

conductive versus convective transfer in the energy equation. It is assumed that convective heat transfer takes place with the velocity obtained by the balance in the momentum equation, and it is defined as:

$$\mathrm{Ra} = \frac{g\beta(T_H - T_C)H^3}{\alpha\nu} = \mathrm{Pr}\frac{g\beta(T_H - T_C)H^3}{\nu^2}, \tag{21}$$

where $g = 9.81\mathrm{m\,s^{-2}}$ is the gravitational acceleration and $H = 1\,\mathrm{m}$ is the domain size. β is the thermal expansion coefficient that is equal to $1/T_{ref}$ for an ideal gas with isobaric expansion (i.e. at constant pressure). In the present study, T_{ref} is taken equal to T_H. Setting Pr= 0.71, the viscosity can be deduced from the target Rayleigh numbers (Eq. 21) of 10^4, 10^5 and 10^6, while the thermal conductivity, λ, in the energy equation is obtained from Eq. (6).

The domain is discretized with a uniform grid with 256×256 cells. The flow is then uniformly initialized as $u_0 = 0$, $T_0 = 300\mathrm{K}$, $\rho_0 = 1.2\,\mathrm{kg\,m^{-3}}$, and $p = p_0 + \rho_0 gy$. The simulation is then carried out until convergence using a time-step, $\delta_t = 6.5 \times 10^{-6}\,\mathrm{s}$.

Figure 2 presents temperature contours as well as streamline patterns, showing a good qualitative agreement with the literature (see[72], e.g.): for $\mathrm{Ra} = 10^4$, the flow is symmetric and dominated by the recirculation in the core region with small eddies near the corner. When increasing the Raleigh number, secondary eddies near the top left and bottom right corners appear and become larger.

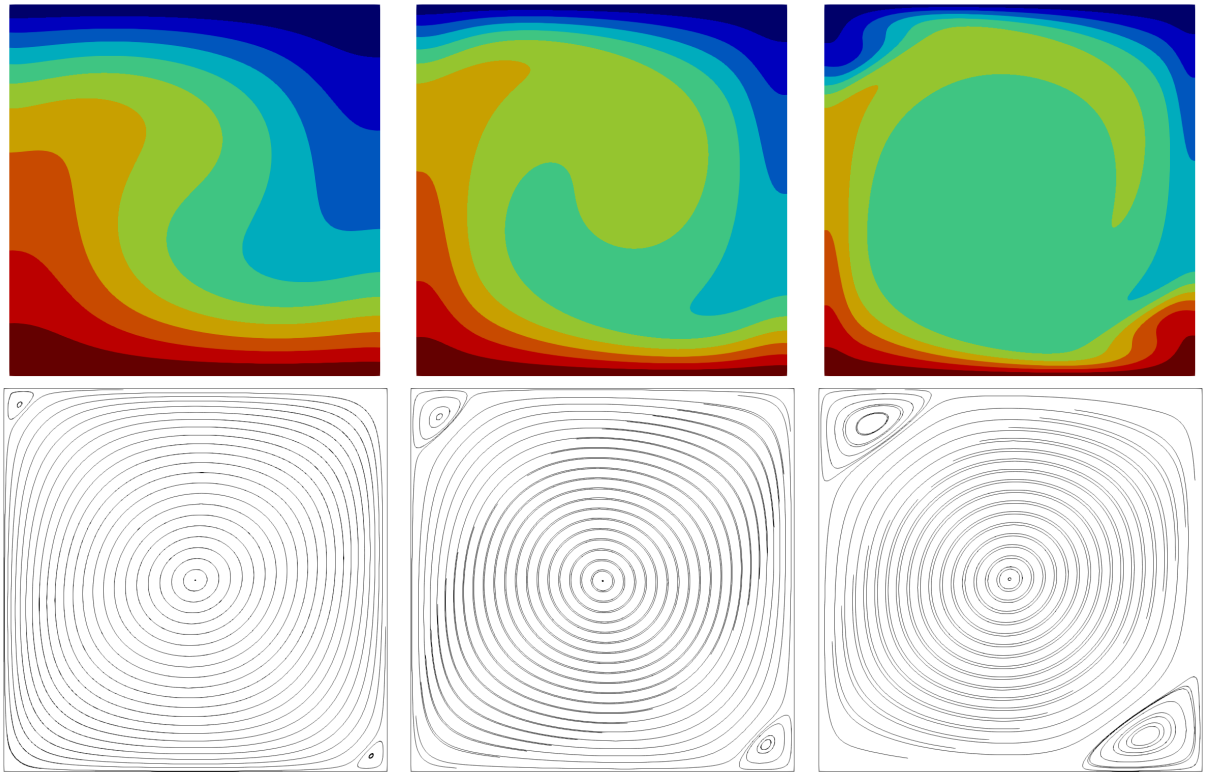

Figure 2: Rayleigh-Benard instability: Temperature contours (top) and streamlines (bottom), for three Rayleigh numbers (10^4, 10^5, 10^6), from left to right.

The quantitative agreement is shown in Fig. 3, presenting velocity profiles along the centerlines. The present numerical results are compared with the benchmark solution provided by Ouertatani et al.[72]. For further validation, the local Nusselt number Nu is calculated at the bottom wall as:

$$\mathrm{Nu} = \left.\frac{\partial T}{\partial y}\right|_{y=0}. \tag{22}$$

It can be observed that both velocity and Nusselt number profiles are in excellent agreement with the reference solutions.

B. Rayleigh-Taylor instability

The Rayleigh-Taylor instability is another classical test case for buoyancy-driven flows due to its practical and fundamental importance. It was investigated extensively in the literature by different numerical methods[73–82]. It consists of two layers of fluids of different densities (ρ_H, ρ_L) at rest under gravitational field, as illustrated in Fig. 4.

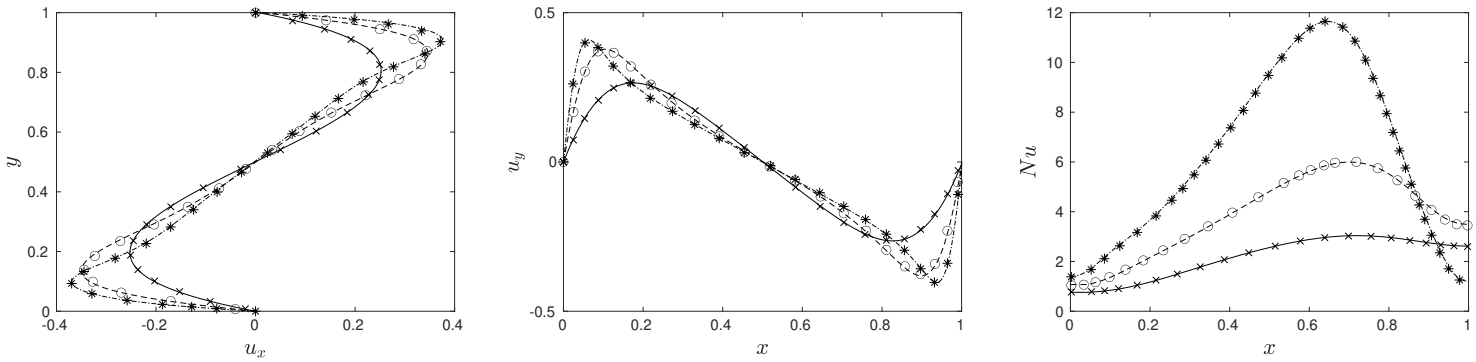

Figure 3: Rayleigh-Benard instability. u_x along the vertical centerline, u_y along the horizontal centerline, and Nusselt number along the bottom wall (from left to right), for Ra=10^4 (solid), Ra=10^5 (dashed) and Ra=10^6 (dot-dashed). Symbols indicate the reference data[72]

.

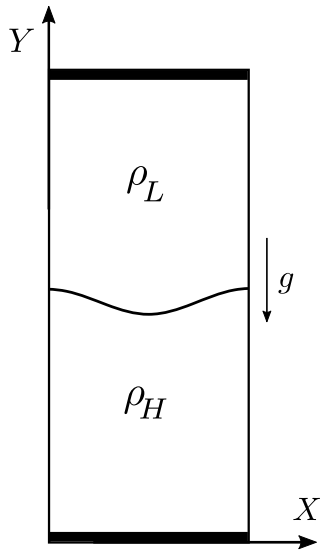

Figure 4: Schematic of Rayleigh Taylor instability.

The dynamics of this problem is governed by the Atwood (At) and Reynolds (Re) numbers:

$$\mathrm{At} = \frac{\rho_H - \rho_L}{\rho_H + \rho_L}, \qquad \mathrm{Re} = \frac{U^* L_x}{\nu}, \tag{23}$$

where L_x is the dimension of the domain in the horizontal direction and $U^* = \sqrt{gL_x}$ is a reference velocity.

The investigated configuration was previously studied in the literature[73–75] with two target

Reynolds numbers of 256 and 2048, The domain size is $L_x \times 4L_x$, discretized with 256×1024 (fine mesh) or 128×512 grid points (coarse mesh). The heavy (index H) and light (index L) fluids are initially separated by a perturbed interface given by the following equation:

$$y_i(x) = \frac{L_x}{10} \cos\left(\frac{2\pi x}{L_x}\right) + 2L_x \tag{24}$$

The fluids initial densities are set to $\rho_H = 3\,\mathrm{kg\,m^{-3}}$ and $\rho_L = 1\,\mathrm{kg\,m^{-3}}$, corresponding to At=0.5. The pressure was initialized to account for the gravity field as follows:

$$p = \begin{cases} p_0 + \rho_L g y, & 0 \le y \le y_i(x) \\ p_0 + \rho_L g y_i(x) + \rho_H g (y - y_i(x)), & y_i(x) < y \end{cases} \tag{25}$$

where p_0 is the pressure at $y = 0$. Finally, the domain size and gravity are set to $L_x = 0.25\mathrm{m}$ and $g = 20\mathrm{m\,s^{-2}}$. The fluid viscosity is obtained from the target Reynolds numbers of 256 and 2048.

Figure 5 represents the density contours obtained for the two Reynolds numbers of 256 and 2048 using the finer mesh. The diagrams of the right of the figure represents the time evolution of the bubble and spike positions. Numerical predictions are compared to reference numerical simulation[73], showing an excellent agreement.

To investigate the robustness of the method, simulations were carried out on the coarser mesh. An excellent agreement is also obtained with a maximum error less than 2%.

III. LARGE EDDY SIMULATION OF A THERMAL PLUME

This Section presents a large eddy simulation of a buoyant plume, generated by a vertical jet of hot air into a quiescent atmosphere. The source conditions correspond to the experiments of Shabbir and George[47], summarized in Table I. The plume source diameter, D, the

$D(m)$	$T_a(K)$	$T_0(K)$	$U_0(m/s)$	$F_0(m^4/s^3)$	$M_0(m^4/s^3)$	$\mathrm{Re} = \frac{U_0 D}{\nu}$	$\mathrm{Fr} = \frac{U_0^2}{gD}$
0.0635	300	568	0.98	0.0127	0.003	1273	1.54

Table I: Source parameters of the plume

exit mean velocity, U_0, the hot air temperature, T_0, and the ambient air temperature, T_a, are 6.35 cm, 0.98 m/s, 568 K and 300 K, respectively. The corresponding Reynolds number, Re,

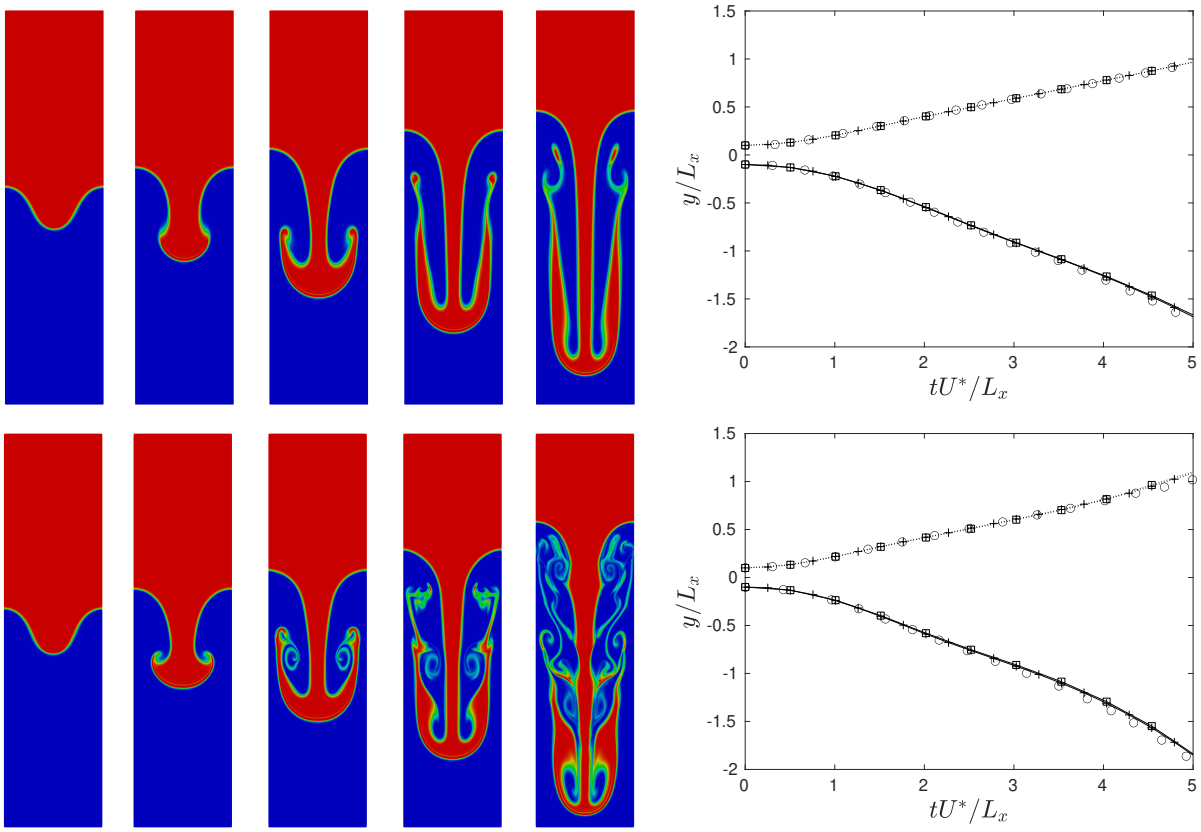

Figure 5: Rayleigh-Taylor instability for Re = 256 (top) and Re = 2048 (bottom). Left: Density contours at different normalized times $t.U^*/L = 1, 2, 3, 4, 5$ obtained for the fine mesh. Right: time evolution of the position of both bubble (solid) and spike dashed). (□) indicates the coarse mesh, (+) for the fine mesh, and (∘) for the reference from He et al.[73].

based on inflow mean injection velocity, source diameter and kinematic viscosity, is 1273. The specific momentum, M_0, buoyancy, F_0, mass, Q_0, and the Morton length scale, L_M, are defined as:

$$F_0 = 2\pi g \int_0^\infty U_z \frac{\Delta T}{T} r dr, \quad M_0 = 2\pi \int_0^\infty U_z^2 r dr, \quad Q_0 = 2\pi \int_0^\infty U_z r dr, \quad L_M = \frac{M_0^{3/4}}{F_0^{1/2}} \tag{26}$$

where r is the radial coordinate. Morton[28] and Morton and Middleton[83] introduced the source parameter Γ_0 that characterizes the plume as being either lazy ($\Gamma_0 > 1$), pure ($\Gamma_0 = 1$) or forced ($0 < \Gamma_0 < 1$):

$$\Gamma_0 = \frac{5Q_0^2 F_0}{8\sqrt{\pi}\alpha M_0^{5/2}} \tag{27}$$

with α the entrainment coefficient explained in details later on. The value of Γ_0 in our

simulation is around 0.9, which indicates a forced plume, having a value of Γ_0 near unity says that the plume is forced but not too much as a result the buoyancy is significant near the source which explains the acceleration zone detailed later.

A. Numerical set-up

The computational domain is a box of size 18D×9D×9D. A uniform mesh, composed of 300×150×150 cells, is considered. The simulation was performed with ProLB on 280 processors. The time-step, based on the sound speed, is $\delta_t = 4.5 \times 10^{-6}$ s. In accordance with previous LES of this configuration[55], the Vreman turbulence model, described in Sec. I B, is applied with a turbulent Prandtl number of $\mathrm{Pr}_t = 0.3$.

The boundary conditions are as follows: at the outlet, a Dirichlet condition is considered for pressure whereas a Neumann condition is applied for other variables with a clip for the axial velocity to prevent any backflow of the plume. Typical inflow/outflow boundary conditions are considered for the vertical sides.

At the inlet, temperature and velocity were imposed to represent a plume source.

For the inlet boundary condition, we followed the strategy of Zhou et al.[55,84] to ensure a transition from laminar to turbulence at a very short distance of the exit, consistently with the experimental observations of Shabbir and George[47]. This kind of fluctuations work more as perturbations with artificial nature so they are not divergence free. However, this does not represent an important issue because the associated time scale is large compared to the flow turbulent time scales (the fastest time scale of our injection is around 0.2s). As a consequence, the impact of this synthetic injection vanishes few diameters away from the inlet where we start performing our analysis. It consists in superimposing azimuthal disturbances:

$$u'(r) = AU_0(r)[(1 - \frac{r}{D}) \sum_{n=1}^{N} \sin(2\pi ft/n) + \frac{r}{D} \sum_{n=1}^{N} \sin(2\pi ft/n + \theta)] \tag{28}$$

to a mean flow $U_0(r)$ corresponding to a pipe profile:

$$U_0(r) = \frac{1}{2} U_0 \left[1 - \tanh(b_2(2r/D - D/2r))\right]. \tag{29}$$

A is the amplitude of the forcing and $N = 6$ is the number of the modes. f is the frequency of the forcing, that is determined by the jet preferred mode corresponding to a Strouhal

number, $\mathrm{St} = fD/U_0$, of 0.3, leading to $f = 4.629$Hz. In the mean pipe flow profile, θ is the azimuthal angle and $b_2 = 6.25$[85].

Note that Eq. (28) was slightly modified from the original formulation[86,87], which presented a singularity at the center. The forcing amplitude $A = 0.2/\sqrt{3}$, corresponds to a RMS fluctuations of 20% for the axial velocity and $A = 0.01/\sqrt{3}$ corresponds to a RMS fluctuations of 1% for the other two components.

The time-averaged statistics (mean, rms,..) presented hereafter were collected over 15 forcing cycles = 20 s once a statistical steady state was reached. The forcing cycle is defined by the longest period of the sine series in Eq. (28) = 1.3 s.

B. Results and discussion

1. Qualitative description

Figure 6 illustrates the transition process trough a snapshot of the three dimensional iso-surface for the Q-criterion[88] along with temperature and density fields. The Q-criterion is defined as:

$$Q = \frac{1}{2}(\|\Omega\|^2 - \|S\|^2), \tag{30}$$

where S and Ω are the strain rate and the vorticity tensor, respectively:

$$\Omega = \frac{1}{2}(\nabla \mathbf{u} + \nabla \mathbf{u}^T), \tag{31}$$

$$S = \frac{1}{2}(\nabla \mathbf{u} - \nabla \mathbf{u}^T), \tag{32}$$

The Q-criterion defines the areas where the vorticity magnitude is larger than the magnitude of the strain rate, such that $Q > 0$ indicates the existence of a vortex.The potential core of the plume becomes rapidly turbulent after few diameters from the source which is consistent with the experimental observations of Shabbir and George[47]. The transition occurs due to the growth of azimuthal instabilities that forms large coherent energy containing structures which eventually break down to generate small-scale turbulence.

Figure 7 shows the energy spectrum based on the axial velocity at distance $z/D = 4$, it shows the energy cascading reported by the theory of Kolmogorov[89] and that we have the

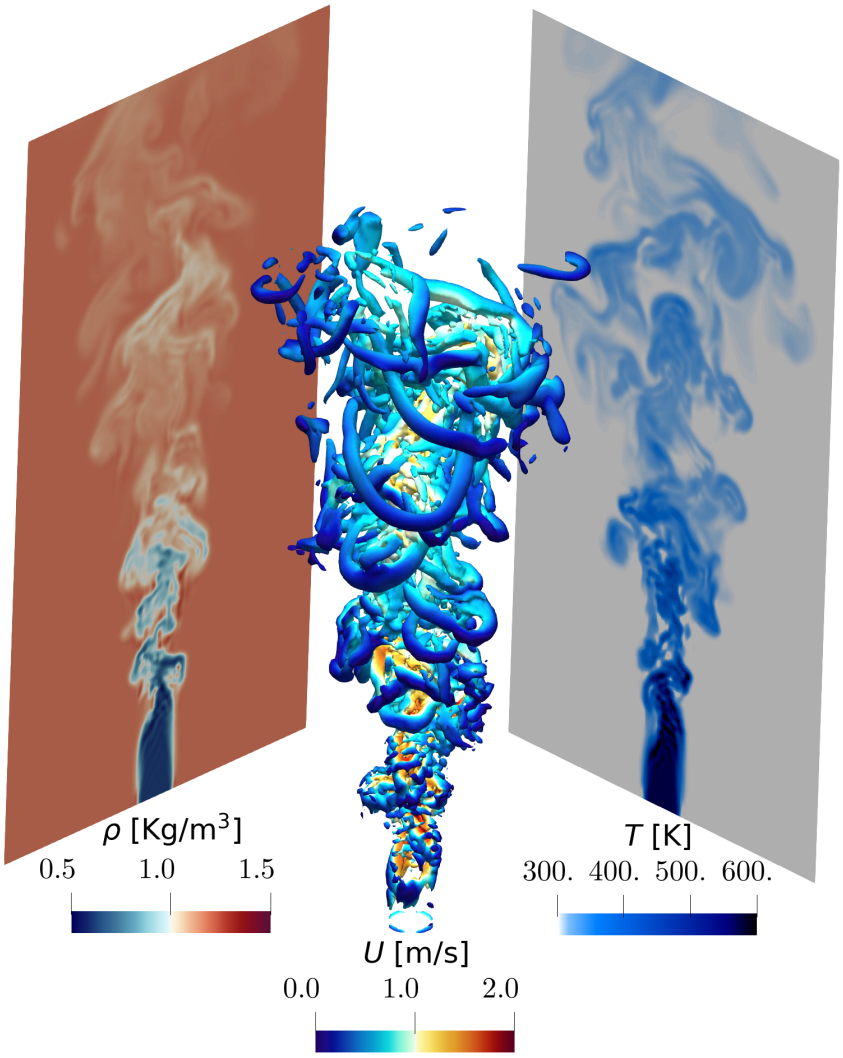

Figure 6: Instantaneous 3D Q-criterion colored by velocity magnitude alongside density and temperature fields

correct power law of $-5/3$ in the inertial range, also the dissipation range was detected at higher frequencies. In addition, in Figure 7 the spectrum for temperature fluctuations is shown, the spectrum initially shows the $-5/3$ power law in the so called inertial-convection region. Afterwards, a region is expected where the spectrum decays sharply and follows a -3 power law, which is a unique characteristic of the forced plumes, and it belongs to

the inertial-diffusive subrange proposed by Papanicolaou & List[46]. Kostovinos[90] argued experimentally that the slope change from $-5/3$ to -3 is due to strong energy feeding as a result of the large plume vortices driven by buoyancy force. This region cannot be clearly identified on the spectrum of temperature fluctuations in Figure 7.

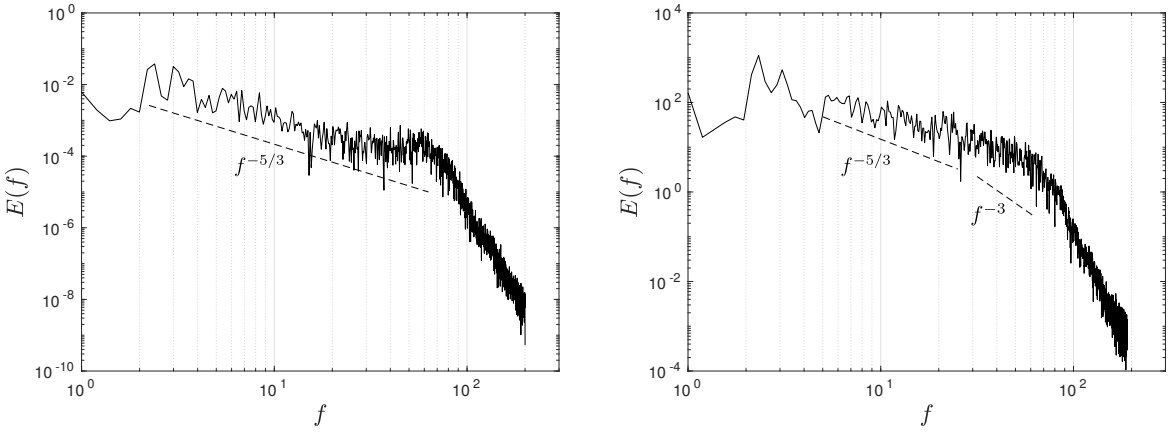

Figure 7: Temporal energy spectrum at $z/D = 4$ for axial velocity (left), temperature (right). Dashed lines indicate the expected characteristic slopes.

2. *Axial mean quantities*

Figure 8 compares the centerline time-averaged axial velocity U_c, and temperature T_c, to the experimental data of Shabbir and George[47], who proposed the following correlation in the plume-like region:

$$U_c = A_U z^{-1/3} F_0^{1/3}, \qquad \frac{T_a}{T_c} = 1 - A_T z^{-5/3} F_0^{2/3}/g, \tag{33}$$

where $A_T = 9.4$ and $A_U = 3.4$ were fitted from the experimental results (see also in Table II). The centerline velocity in Fig. 8 increases rapidly from its initial value at the inlet to a maximum value of about 1.8 at $z/D \approx 2.5$ and then decreases afterwards rapidly to reach values lower than the inflow velocity after about 6 diameters. This behavior was also observed by Lingens et al.[91] who experimentally investigated buoyant jet diffusion flame. The initial acceleration in the near field is due to the large buoyancy force resulting from large temperature (density) difference between the plume core and the ambient. The rapid deceleration after the peak results from the turbulent mixing of the plume with the surrounding

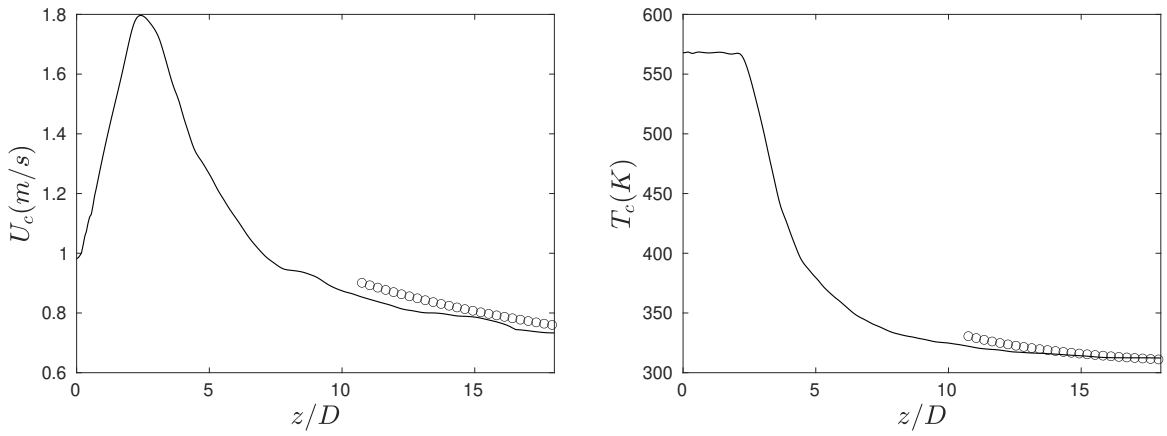

Figure 8: Centerline mean axial velocity (left), and Temperature (right) profiles. Solid line for the simulation, symbols for experimental data of Shabbir and George[47]

fluid, which decreases the temperature. The rapid decrease in temperature downstream the potential core is clearly evidenced in Fig. 8. The location of the transition from jet-like to plume-like behavior can be identified through the rates of decrease which have to scale with $z^{-1/3}$ and $z^{-5/3}$ for velocity and temperature, respectively. The numerical model predicts the transition at $z/D \approx$ 10-11 which is consistent with the experiments of Shabbir and Georges[47] where it was estimated to occur at $z/D = 10.5$. In the plume-like region, the model reproduces quantitatively the evolution of both axial velocity and temperature with z/D, although U_c is on the whole slightly underestimated.

The non-dimensional mean axial velocity $U_c z/\sqrt{M_0}$ is plotted as a function of the non-dimensional axial distance $\xi = z/L_M$ in Fig. 9. The transition to the plume-like region (i.e. the slope change) is predicted around $\xi = 4 \sim 5$ which is consistent with the finding of Morton et al.[43] who reported that a forced plume will reach a pure plume behavior for $z/L_M > 5$. In addition, our simulation exhibits a good agreement with the experimental profile obtained from the correlation of Shabbir and George[47] (see Eq. 33) in the plume-like region.

Forced plumes becomes plume-like far away from the source in homogeneous environment even if the injected momentum flux is large when the function Γ changes from a value smaller than 1 at the source to a value of 1 in the far field. Four regions were identified in the present simulation: 1) a non-buoyant region where momentum dominates the flow, 2) an acceleration region where the plume is accelerated due to gravity, 3) an intermediate

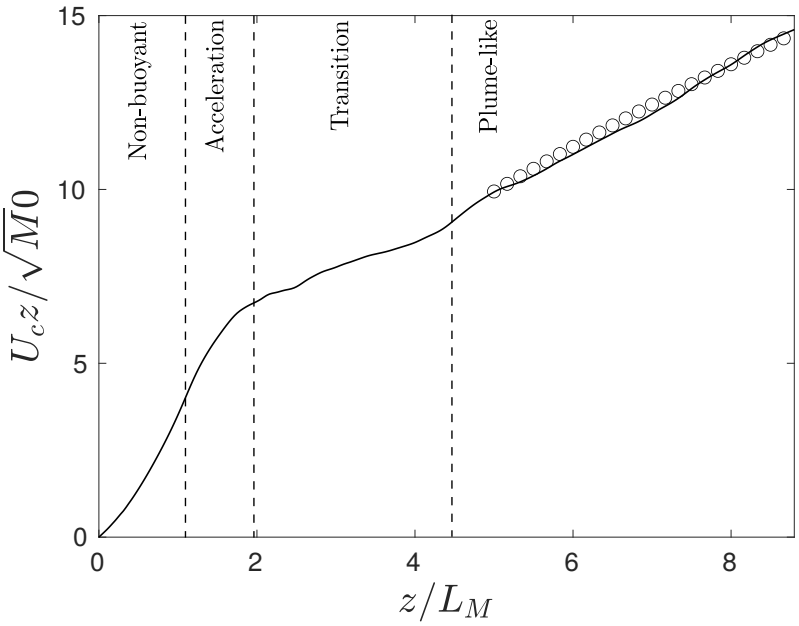

Figure 9: Centerline mean non-dimensional axial velocity profile. Solid line for the simulation and symbols for experiment of Shabbir and George[47]

region where influence of initial momentum weakens, and 4) the plume-like region (i.e. self-similarity region) where the plume dynamics is dominated solely by the buoyancy forces. This picture is consistent with the descriptions of Gebhart et al.[92] and Chen and Rodi[93] although they did not report the acceleration region (i.e. region 2). Note that the limits of each region in Fig. 9 are defined using the velocity inflection points, consistently with the global behavior of the plume.

3. Fluctuations quantities

In this section, the axial evolution of the rms values of axial velocity and temperature fluctuations and the cross-correlation between velocity and temperature fluctuations are discussed and compared with experiments[45–48], for which the fitting parameters are reported in Tab. II.

Figure 10 presents the rms values of axial velocity and temperature fluctuations. As expected, the velocity fluctuations are about 20% at vicinity of the inflow plane and corresponds to the imposed disturbance level. The velocity fluctuations decrease in the potential core region of the plume before starting to increase very abruptly in the laminar to turbu-

Reference	A_T	A_U	B_T	B_U	$\overline{(T'^2)}^{1/2}/\overline{\Delta T_c}$	$\overline{(u_z'^2)}^{1/2}/\overline{U_c}$	$\overline{u_z'T'}/\overline{(u_z'^2)}^{1/2}\overline{(T'^2)}^{1/2}$
Shabbir & George[47]	9.4	3.4	68	58	0.4	0.33	0.67
George et al.[45]	9.1	3.4	65	55	0.38	0.28	0.67
Papanicolaou & List[46]	14.28	3.85	80	90	0.42	0.25	0.51
Nakagome & Hirata[48]	11.5	3.89	48.1	63	0.36	0.25	0.46

Table II: Summary of mean flow parameters and turbulence intensities for different experiments

lence transition region, the initial drop in velocity fluctuations is due to the artificial nature of the fluctuations imposed at the inlet. These artificial fluctuations, without a proper cascade, are dissipated very quickly; however, they constitute the seed for a correct transition to turbulence with a realistic energy cascade in the far field where we perform our analysis. In the plume-like region, both velocity and temperature fluctuations decrease at a same rate as mean velocity and temperature to ensure constant ratio of $\overline{u'^2}^{1/2}/U_c$ and $\overline{T'^2}^{1/2}/(T_c - T_a)$. The predicted velocity-based turbulence intensity in the plume-like region is lower than those of 0.28 and 0.33 reported by George et al.[45] and Shabbir and George[47], respectively. It is in better agreement with those of 0.25 reported by Papanicolaou and List[46] and Nakagome and Hirata[48]. On the other hand, Fig. 10 shows that the temperature-based turbulence intensity is also consistent with the available data.

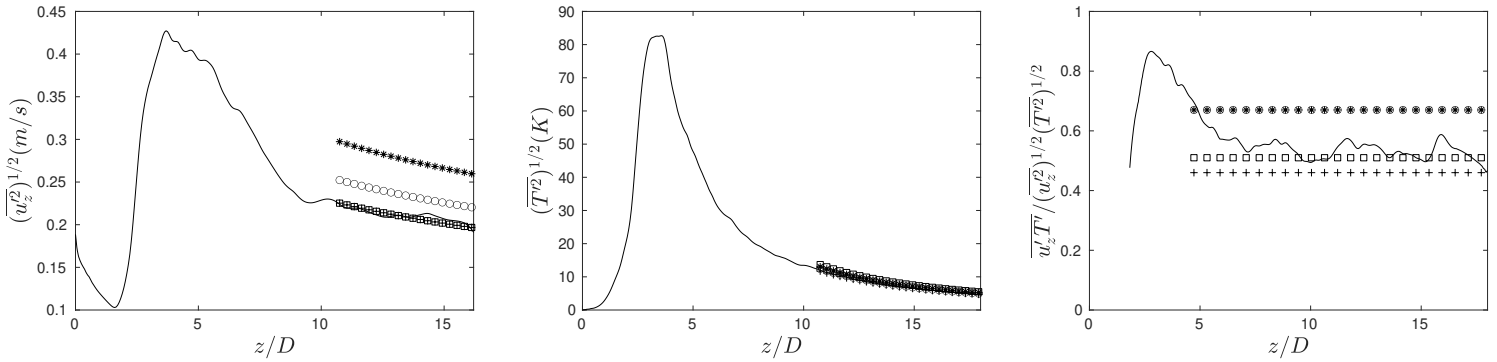

Figure 10: Center line profiles of r.m.s of axial velocity (left), temperature (center), and the cross-correlation of velocity and temperature fluctuations (right). Solid line for simulation, ($*$) for Shabbir & George[47], ($\circ$) for Geroge et al.[45], ($\square$) for Papanicolaou & List[46], and ($+$) for Nakagome & Hirata[48].

Figure 10 shows the evolution of the cross correlation between velocity and temperature fluctuations, $\overline{u'T'}/(\overline{(u'^2)}^{1/2}\overline{(T'^2)}^{1/2}$, along the center line. It can be clearly observed that velocity and temperature fields are positively correlated in this type of flows with a predicted nearly constant value in plume-like region of about 0.55. This value is lower that those reported by George and co-workers[45,47] in the range 0.6-0.7, averaged to 0.67 (see Table II), and in closer agreement with those of 0.46 and 0.51 reported by Nakagome and Hirata[48] and Papanicolaou and List[46], respectively.

4. Self-similarity

An important feature of the mean flow in the fully-developed region of turbulent positively buoyant plumes is the "self-similarity" or "self-preserving" behaviour. The radial mean velocity and temperature profiles follow a Gaussian shape and become wider as the plume rises. The profiles collapse on the same curve when considering appropriate dimensionless variables:

$$\frac{U_z}{U_c} = \exp\left\{(-B_u\frac{r^2}{z^2})\right\}, \qquad \frac{T-T_a}{T_c-T_a} = \exp\left\{(-B_T\frac{r^2}{z^2})\right\} \tag{34}$$

The coefficients B_u and B_T are unknown empirical constants that can be obtained by assuming a linear growth of the plume width b[43]:

$$\frac{b}{z} = \frac{6}{5}\alpha = const, \tag{35}$$

The coefficients will then be calculated using $B_u = \sqrt{z/b_u}$ and $B_T = \sqrt{z/b_T}$, where b_u and b_T are the plume width defined by the distance from the centerline to the point at which we have $1/e$ of the centerline values of velocity and temperature, respectively. George et al.[45] determined by experiments those coefficients as $B_u = 55$ and $B_T = 65$.

The radial profiles of mean velocity and temperature from our LES at $z/D = 10, 12, 14, 16$ and the profiles of George et al.[45] form are plotted in Fig. 11. The velocity and the temperature rise above the ambient are normalized by the centreline value. The profiles are plotted versus the non-dimensional radial coordinate $r/(z+z_0)$ where z_0 is the virtual origin of the plume. Empirical relationships were reported to estimate the location of the virtual origin[55]. As pointed out by Yang[56], the location of virtual origin predicted in the simulation can be different from that estimated by empirical formula. Indeed, this location

is significantly affected by the transition from laminar to turbulent whose the prediction is a difficult task in LES mainly due to its sensitivity to the plume's source inflow condition. In the present study, the virtual origin was estimated to collapse the radial profiles in the fully developed region to a single dimensionless Gaussian profile following the methodology proposed by Yan[56], giving z_0 set equal to $2.3D$. It can be observed in Fig. 11 that the self-similarity is well preserved in the simulation and the predicted self-similarity profiles agree well with those reported by Georges et al.[45].

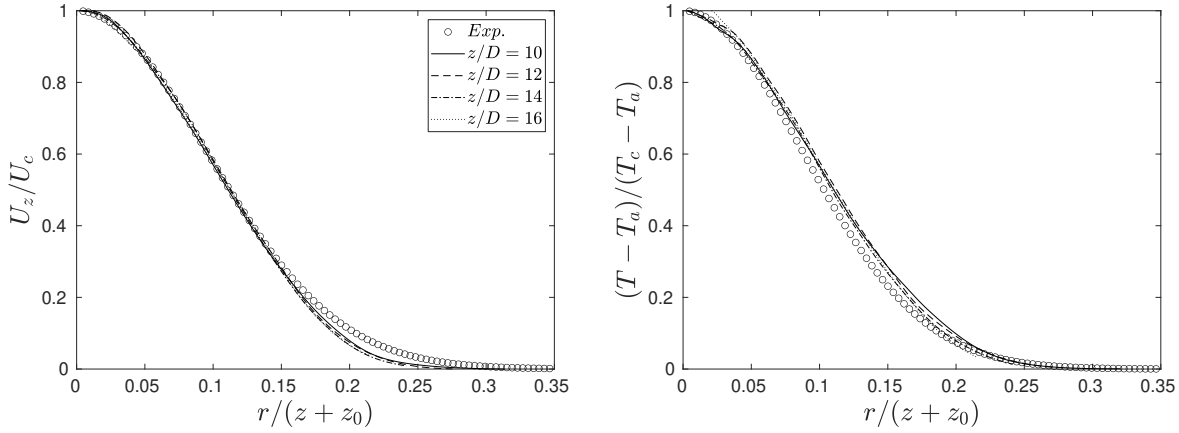

Figure 11: Radial profiles of mean axial velocity (left) ,and mean temperature (right) at four axial positions compared to the experiments of George et al.[45]

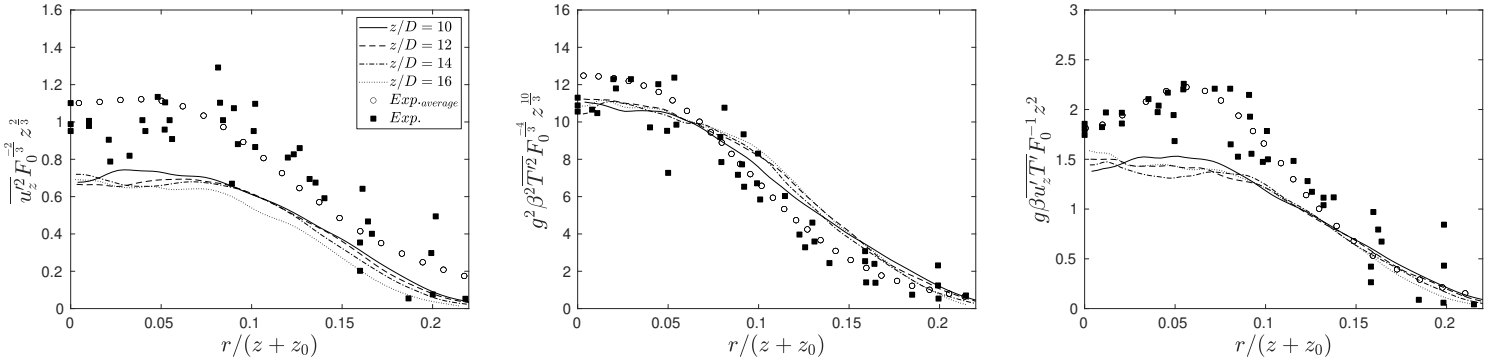

Figure 12: Radial profiles at $z/D = 10, 12, 14, 16$ for normalized r.m.s of axial velocity fluctuation (left), r.m.s of temperature fluctuations (middle), and cross correlation of both velocity and temperature fluctuations (right).

Following Shabbir & George[47], the radial profiles of r.m.s values of axial velocity and temperature and of the cross correlation between velocity and temperature fluctuations are

plotted in terms of the similarity variables in Fig. 12. The predicted profiles clearly exhibit a self-similar behavior. The agreement with the experimental data is reasonable although, consistently with Fig. 10, both r.m.s values of axial velocity fluctuations and the cross correlation between velocity and temperature fluctuations are overall underestimated.

5. *Entrainment*

The mechanism of turbulent mixing which brings air into the buoyant plume is called entrainment. The ideal plume theory is based on both Boussinesq and top-hat radial-profile assumptions and assumes that the mean entrained flux across the edge of the plume E (entrainment rate) is proportional to the local upward velocity W. An air entrainement coefficient is then defined as:

$$\alpha = \frac{E}{bW} \tag{36}$$

where E, W, b are know as the top-hat variables of entrainment rate, local vertical velocity and plume width defined by Turner[94]:

$$b^2W = \int_0^\infty U_z r dr, \qquad b^2W^2 = \int_0^\infty U_z^2 r dr, \qquad E = \frac{d}{dz}\left(\int_0^\infty U_z r dr\right) \tag{37}$$

The Plume width, b, can be calculated as the value at which velocity or temperature reaches a value of $1/e$ of the centerline value as indicated by Morton et al.[43]. This will be referred to as (*method 1*) hereafter. It can be also obtained from Eq. 37, as $b^2W/\sqrt{b^2W^2}$. This second method will referred to as (*method 2*) hereafter. Figure 13 compares the two methods. The experimental slope obtained by George et al.[45] and the numerical prediction obtained by Zhou et al.[55] are also plotted in Fig. 13. Both the present predicted velocity and temperature half-widths decrease first due to the "necking" process in the near field, as observed experimentally by Cetegen[95], before, as expected, increasing almost linearly in plume region. The two methods provide on the whole consistent predictions that agree with both the experimental slope and the numerical results obtained by Zhou et al.[55].

The entrainment coefficient, α, can be calculated using Eq. 35. This method requires the knowledge the width of b, along the plume axis. It can be obtained either from temperature and velocity radial profiles (*method 1*) or from Eq. 37 (*method 2*), as discussed previously. Another method was adopted by Zhou et al.[55] from Eqs. 36 and 37, leading to

$\alpha = E/\sqrt{b^2W^2}$. This method will be referred to as (*method 3*). Figure 13 shows that the three methods provide consistent results in the far-field. Our results agrees well with the LES of Zhou et al.[55] which settles on a constant value in the far-field, $\alpha = 0.09 - 0.1$. Our predictions of α in the plume region are also close to the value of 0.116 adopted by Morton in his plume model[28] and the experimental value 0.108 reported by George et al.[45].

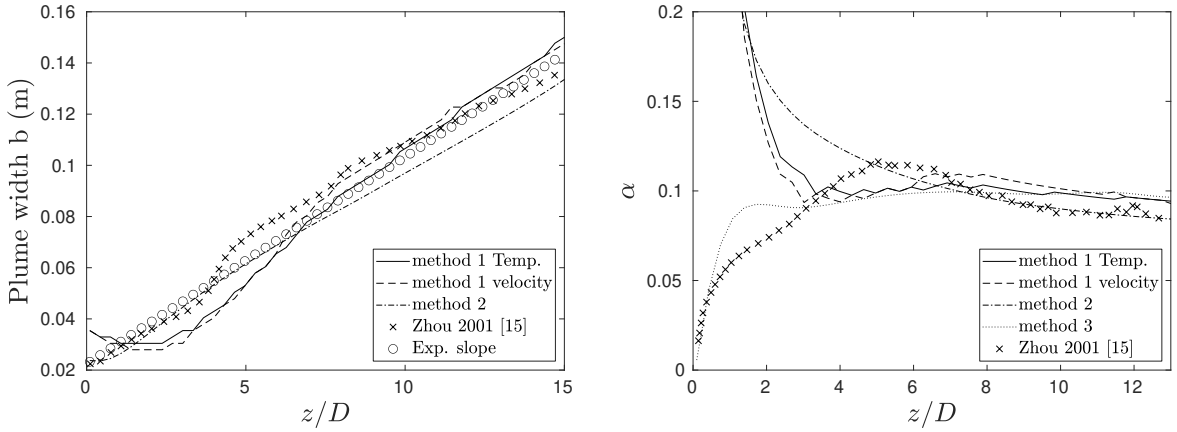

Figure 13: Evolution with the height of (left) the plume width and (right) the entrainment coefficient α

Integrating radially the momentum and energy equations across the flow introduces two fundamental quantities[47]. The first is the momentum flux, M that can be normalized by the inflow momentum flux, M_0 (see Table I):

$$M = 2\pi \int_0^\infty (U_z^2 + \overline{u_z'^2} - \overline{v'^2}) r dr \tag{38}$$

The moment flux ratio increases with the height according to the following relationship[96]:

$$\frac{M}{M_0} = k(\frac{x}{L_M})^{4/3} \tag{39}$$

Different values of 0.35[96], 0.34[47] and 0.29[46] were reported for the coefficient k. Fig. 14 compares our result to these experimental results. Model predictions are in good agreement with the experiments of Shabbir and George[47] and Fisher[96] but overpredict that of Papanicolaou and List[46].

The second is the buoyancy flux F, that has to be conserved conserved along the plume

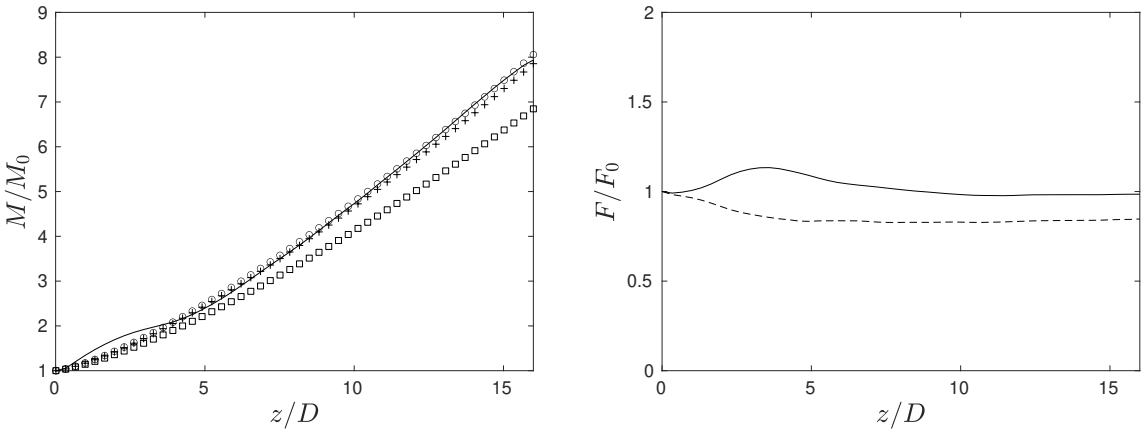

Figure 14: Axial profile of momentum flux ratio (left). The solid line represents the present LES, whereas the symbols represent the experimental data of Fischer et al.[96] ($\circ$), ($+$) for Shabbir & George[47] and ($\square$) for Papanicolaou & List[46]. Axial profile of buoyancy flux ratio (right), solid line includes the turbulent heat flux while dash line does not.

height:

$$F = 2\pi g \int_0^\infty (U_z \frac{\Delta T}{T} + \frac{\overline{u_z' T'}}{T}) r dr \tag{40}$$

The buoyancy flux is normalized by its injection value, F_0. Figure 14 shows the evolution of F/F_0 along the plume height. The simulated normalized buoyancy flux evolves around unity, consistently with the theory (solid line). It appears clearly by comparing the solid and dashed lines that the turbulent contribution is essential. When it is disregarded, the buoyancy flux decreases with the axial distance and is no more conserved. The turbulence contribution is predicted around $15\% - 20\%$ as also noted by Shabbir & George[47], while George et al.[45] and Papanicolaou & List[46] found the contribution to be about 15%.

IV. CONCLUDING REMARKS

A recursive regularized pressure based LBM solver (ProLB) was tested for buoyancy driven flows.

The solver was able to correctly validate the Rayleigh Bénard cavity test case for different Rayleigh numbers $Ra = 10^4, 10^5, 10^6$, vertical and horizontal velocity profiles as well

as Nusslet number profiles at the bottom wall were all in a good agreement with the reference.

As for the Rayleigh Taylor test case, we were able to correctly predict the instantaneous evolution of the positions of bubble and spike for two different Reynolds numbers $\mathrm{Re} = 256, 2048$. In addition, the test case was run on a coarser mesh to test the robustness of the solver and the results were abundantly satisfying.

For the 3d forced plume simulation, which is a critical test case in which the buoyancy is highly coupled with momentum and turbulent mixing, the solver was able to anticipate the correct physics of a thermal plume from numerous aspects listed below:

- The velocity energy spectrum follows the Kolmogorov theoretical slope of $-5/3$ indicating a proper resolution of the turbulence energy cascading as reported in the literature.

- Axial profiles of mean velocity and temperature were in a good agreement with the experimental data.

- Our forced-plume reaches a plume-like region at around $z/L_m = 4 \approx 5$ which is consistent with the findings in the literature.

- The axial profiles of rms for velocity and temperature also were in a good agreement with the experiments, we should emphasize that we did not take into account the experimental errors which are significant specially for the second order statistics.

- The cross-correlation between velocity and temperature has a high positive value which compares well with the reported values from experiments and indicates a strong coupling between the velocity and temperature fluctuations due to gravity.

- Self similarity profiles in the far field (i.e. plume-like region) were achieved for both mean and rms of velocity and temperature.

- The growth rate of the plume was examined through the spatial evolution of the plume width. The growth of the plume compared very well with experimental and numerical references.

- The entrainment of fluid form the surrounding was correctly predicted by examining the entrainment coefficient α, and the predictions were in a good agreement with the theoretical, experimental and numerical references.

- Integral quantities, mainly Buoyancy flux and momentum flux, were compared with the experiments and both were in a good agreement, we emphasize about the finding that the turbulent heat flux participates by around 20% in the total buoyancy flux which is consistent with the experiments.

From all the previous points we can conclude that our solver is capable of reproducing the physics of a thermal plume correctly whether the mean values, the second order statistics or even integral quantities through the plume, and that our code can handle any type of flows with variable densities regardless of their complexity.

ACKNOWLEDGEMENTS

Centre de Calcul Intensif d'Aix-Marseille and GENCI-TGCC/CINES (Grants 2021-A0092B11951, 2021-A0092A07679) are acknowledged for granting access to their high performance computing resources.

DATA AVAILABILITY

The data that support the findings of this study are available from the corresponding author upon reasonable request.

REFERENCES

[1]S. Chen and G. D. Doolen, "Lattice boltzmann method for fluid flows," Annual review of fluid mechanics **30**, 329–364 (1998).

[2]P. Boivin, M. Tayyab, and S. Zhao, "Benchmarking a lattice-boltzmann solver for reactive flows: Is the method worth the effort for combustion?" Physics of Fluids **33**, 017703 (2021).

[3]S. Succi, R. Benzi, and F. Higuera, "The lattice boltzmann equation: a new tool for computational fluid-dynamics," Physica D: Nonlinear Phenomena **47**, 219–230 (1991).

[4]Z. Guo and C. Shu, *Lattice Boltzmann method and its applications in engineering*, Vol. 3 (World Scientific, 2013).

[5]T. Krüger, H. Kusumaatmaja, A. Kuzmin, O. Shardt, G. Silva, and E. M. Viggen, *The Lattice Boltzmann Method: Principles and Practice* (Springer, 2016).

[6]P. L. Bhatnagar, E. P. Gross, and M. Krook, "A model for collision processes in gases. i. small amplitude processes in charged and neutral one-component systems," Physical review **94**, 511 (1954).

[7]D. d. Humières, I. Ginzburg, M. Krafczyk, P. Lallemand, and L.-S. Luo, "Multiple–relaxation–time lattice Boltzmann models in three dimensions," Phil. Trans. R. Soc. Lond. A **360**, 437–451 (2002).

[8]O. Malaspinas, "Increasing stability and accuracy of the lattice boltzmann scheme: recursivity and regularization," arXiv preprint arXiv:1505.06900 (2015).

[9]J. Jacob, O. Malaspinas, and P. Sagaut, "A new hybrid recursive regularised bhatnagar–gross–krook collision model for lattice boltzmann method-based large eddy simulation," Journal of Turbulence **19**, 1051–1076 (2018).

[10]S. A. Hosseini, A. Eshghinejadfard, N. Darabiha, and D. Thévenin, "Weakly compressible lattice boltzmann simulations of reacting flows with detailed thermo-chemical models," Computers & Mathematics with Applications **79**, 141–158 (2020).

[11]M. Saadat, S. Hosseini, B. Dorschner, and I. Karlin, "Extended lattice boltzmann model for gas dynamics," Physics of Fluids **33**, 046104 (2021).

[12]Y. Feng, P. Sagaut, and W. Tao, "A three dimensional lattice model for thermal compressible flow on standard lattices," Journal of Computational Physics **303**, 514–529 (2015).

[13]Y. Feng, P. Sagaut, and W.-Q. Tao, "A compressible lattice boltzmann finite volume model for high subsonic and transonic flows on regular lattices," Computers & Fluids **131**, 45–55 (2016).

[14]Y. Feng, P. Boivin, J. Jacob, and P. Sagaut, "Hybrid recursive regularized thermal lattice boltzmann model for high subsonic compressible flows," Journal of Computational Physics **394**, 82 – 99 (2019).

[15]S. Guo, Y. Feng, J. Jacob, F. Renard, and P. Sagaut, "An efficient lattice boltzmann method for compressible aerodynamics on d3q19 lattice," Journal of Computational Physics , 109570 (2020).

[16]G. Farag, S. Zhao, T. Coratger, P. Boivin, G. Chiavassa, and P. Sagaut, "A pressure-based regularized lattice-boltzmann method for the simulation of compressible flows," Physics of Fluids **32**, 066106 (2020).

[17]G. Farag, T. Coratger, G. Wissocq, S. Zhao, P. Boivin, and P. Sagaut, "A unified hybrid lattice-boltzmann method for compressible flows: bridging between pressure-based and density-based methods," Physics of Fluids **33** (2021).

[18]Y. Feng, P. Boivin, J. Jacob, and P. Sagaut, "Hybrid recursive regularized thermal lattice boltzmann model for high subsonic compressible flows," Journal of Computational Physics **394**, 82–99 (2019).

[19]I. Cheylan, S. Zhao, P. Boivin, and P. Sagaut, "Compressible pressure-based lattice-boltzmann applied to humid air with phase change," Applied Thermal Engineering , 116868 (2021).

[20]J. Jacob and P. Sagaut, "Wind comfort assessment by means of large eddy simulation with lattice boltzmann method in full scale city area," Building and Environment **139**, 110–124 (2018).

[21]L. Merlier, J. Jacob, and P. Sagaut, "Lattice-boltzmann large-eddy simulation of pollutant dispersion in street canyons including tree planting effects," Atmospheric Environment **195**, 89–103 (2018).

[22]L. Merlier, J. Jacob, and P. Sagaut, "Lattice-boltzmann large-eddy simulation of pollutant dispersion in complex urban environment with dense gas effect: Model evaluation and flow analysis," Building and Environment **148**, 634–652 (2019).

[23]M. Tayyab, B. Radisson, C. Almarcha, B. Denet, and P. Boivin, "Experimental and numerical lattice-boltzmann investigation of the darrieus-landau instability," Combustion and Flame **221**, 103–109 (2020).

[24]M. Tayyab, S. Zhao, Y. Feng, and P. Boivin, "Hybrid regularized lattice-boltzmann modelling of premixed and non-premixed combustion processes," Combustion and Flame **211**, 173–184 (2020).

[25]M. Tayyab, S. Zhao, and P. Boivin, "Lattice-boltzmann modelling of a turbulent bluff-body stabilized flame," Physics of Fluids **33**, 031701 (2021).

[26]S. P. Domino, J. Hewson, R. Knaus, and M. Hansen, "Predicting large-scale pool fire dynamics using an unsteady flamelet- and large-eddy simulation-based model suite," Physics of Fluids **33**, 085109 (2021).

[27]B. Morton, "Buoyant plumes in a moist atmosphere," Journal of Fluid Mechanics **2**, 127–144 (1957).

[28]B. . Morton, "Forced plumes," Journal of Fluid mechanics **5**, 151–163 (1959).

[29]A. W. Woods, "Turbulent plumes in nature," Annual Review of Fluid Mechanics **42**, 391–412 (2010).

[30]G. Heskestad, "Engineering relations for fire plumes," Fire Safety J. **7**, 25–32 (1984).

[31]M. D. Fromm and R. Servranckx, "Transport of forest fire smoke above the tropopause by supercell convection," Geophysical Research Letters **30** (2003).

[32]R. A. Kahn, Y. Chen, D. L. Nelson, F.-Y. Leung, Q. Li, D. J. Diner, and J. A. Logan, "Wildfire smoke injection heights: Two perspectives from space," Geophysical Research Letters **35** (2008).

[33]D. Pyle, "Sparks, r. s. j., bursik, m. i., carey, s. n., gilbert, j. s., glaze, l. s., sigurdsson, h. & woods, a. w. 1997. volcanic plumes. xv 574 pp. chichester, new york, weinheim, brisbane, singapore, toronto: John wiley & sons. price £85.00 (hard covers). isbn 0 471 93901 3." Geological Magazine **135**, 143–158 (1998).

[34]G. G. Ernst, R. S. J. Sparks, S. N. Carey, and M. I. Bursik, "Sedimentation from turbulent jets and plumes," Journal of Geophysical Research: Solid Earth **101**, 5575–5589 (1996).

[35]G. Carazzo, E. Kaminski, and S. Tait, "On the rise of turbulent plumes: Quantitative effects of variable entrainment for submarine hydrothermal vents, terrestrial and extra terrestrial explosive volcanism," Journal of Geophysical Research: Solid Earth **113** (2008).

[36]E. D. Skyllingstad and D. W. Denbo, "Turbulence beneath sea ice and leads: A coupled sea ice/large-eddy simulation study," Journal of Geophysical Research: Oceans **106**, 2477–2497 (2001).

[37]K. Widell, I. Fer, and P. M. Haugan, "Salt release from warming sea ice," Geophysical research letters **33** (2006).

[38]G. A. Briggs, "Chimney plumes in neutral and stable surroundings," Atmospheric Environment (1967) **6**, 507–510 (1972).

[39]B. Fisher, "Predicting cooling tower plume dispersion," Proceedings of the Institution of Mechanical Engineers, Part A: Journal of Power and Energy **211**, 291–297 (1997).

[40]C. J. Chen and W. Rodi, *Vertical buoyant jets: a review of experimental data* (Pergamon, 1980).

[41]W. Schmidt, "Turbulent propagation of a stream of heated air," Z. angew. math. mech **21**, 265–278 (1941).

[42]H. Rouse, C. S. Yih, and H. Humphreys, "Gravitational convection from a boundary source," Tellus **4**, 201–210 (1952).

[43]B. Morton, G. I. Taylor, and J. S. Turner, "Turbulent gravitational convection from maintained and instantaneous sources," Proceedings of the Royal Society of London. Series A. Mathematical and Physical Sciences **234**, 1–23 (1956).

[44]G. Heskestad, "Dynamics of the fire plume," Phil. Trans. R. Soc. Lond. A **356**, 2815–2833 (1998).

[45]W. K. George Jr, R. L. Alpert, and F. Tamanini, "Turbulence measurements in an axisymmetric buoyant plume," International Journal of Heat and Mass Transfer **20**, 1145–1154 (1977).

[46]P. N. Papanicolaou and E. J. List, "Investigations of round vertical turbulent buoyant jets," Journal of Fluid Mechanics **195**, 341–391 (1988).

[47]A. Shabbir and W. K. George, "Experiments on a round turbulent buoyant plume," Journal of Fluid Mechanics **275**, 1–32 (1994).

[48]H. Nakagome and M. Hirata, "The structure of turbulent diffusion in an axisymmetrical thermal plume," in *Proc. 1976 ICHMT Seminar on Turbulent Buoyant Convection* (1977) pp. 361–372.

[49]Z. Dai, L. Tseng, and G. Faeth, "Structure of round, fully-developed, buoyant turbulent plumes," J. Heat Transf. **116**, 409–417 (1994).

[50]Z. Saeed, E. Weidner, B. Johnson, and T. L. Mandel, "Buoyancy-modified entrainment in plumes: Theoretical predictions," Physics of Fluids **34**, 015112 (2022).

[51]S. Nam and R. G. J. Bill, "Numerical simulation of thermal plumes," Fire Safety J. **21**, 213–256 (1993).

[52]J. Worthy, V. Sanderson, and P. Rubini, "Comparison of modified k-epsilon turbulence models for buoyant plumes," Num. Heat Transf. B **39**, 151–165 (2001).

[53]C. P. Brescianini and M. Delichatsios, "New evaluation of the k-epsilon turbulence model for free buoyant plumes," Num. Heat Transf. A: Fundamentals **43**, 731–751 (2003).

[54]Z. H. Yan, "Application of two buoyancy modified k-epsilon turbulence models to different types of buoyant plumes," Fire Safety J. **41**, 122–138 (2006).

[55]X. Zhou, K. H. Luo, and J. J. Williams, "Large-eddy simulation of a turbulent forced plume," European Journal of Mechanics-B/Fluids **20**, 233–254 (2001).

[56]Z. H. Yan, "Large eddy simulations of a turbulent thermal plume," Heat Mass Transfer **43**, 503–514 (2007).

[57]C. Pant and A. Bhattacharya, "Evaluation of an energy consistent entrainment model for volumetrically forced jets using large eddy simulations," Physics of Fluids **30**, 105107 (2018).

[58]E. Kaminski, S. Tait, and G. Carazzo, "Turbulent entrainment in jets with arbitrary buoyancy," Journal of Fluid Mechanics **526**, 361–376 (2005).

[59]M. van Reeuwijk and J. Craske, "Energy-consistent entrainment relations for jets and plumes," Journal of Fluid Mechanics **782**, 333–355 (2015).

[60]M. V. Pham, F. Plourde, S. D. Kim, and S. Balachandar, "Large-eddy simulation of a pure thermal plume under rotating conditions," Physics of Fluids **18**, 015101 (2006).

[61]F. Plourde, M. V. Pham, S. D. Kim, and S. Balachandar, "Direct numerical simulations of a rapidly expanding thermal plume: structure and entrainment interaction," Journal of Fluid Mechanics **604**, 99 (2008).

[62]C. H. Chen and K. Bhaganagar, "New findings in vorticity dynamics of turbulent buoyant plumes," Physics of Fluids **33**, 115104 (2021).

[63]K. Bhaganagar and S. R. Bhimireddy, "Numerical investigation of starting turbulent buoyant plumes released in neutral atmosphere," Journal of Fluid Mechanics **900**, A32 (2020).

[64]CS Communication & Systèmes, "Prolb," .

[65]A. Vreman, "An eddy-viscosity subgrid-scale model for turbulent shear flow: Algebraic theory and applications," Physics of fluids **16**, 3670–3681 (2004).

[66]T. Poinsot and D. Veynante, *Theoretical and numerical combustion* (RT Edwards, Inc., 2005).

[67]T. Krüger, H. Kusumaatmaja, A. Kuzmin, O. Shardt, G. Silva, and E. M. Viggen, "The lattice boltzmann method," Springer International Publishing **10**, 4–15 (2017).

[68]G. Farag, S. Zhao, G. Chiavassa, and P. Boivin, "Consistency study of lattice-boltzmann schemes macroscopic limit," Physics of Fluids **33**, 031701 (2021).

[69]G. Wissocq and P. Sagaut, "Hydrodynamic limits and numerical errors of isothermal lattice boltzmann schemes," Journal of Computational Physics **450**, 110858 (2022).

[70]T. Coratger, G. Farag, S. Zhao, P. Boivin, and P. Sagaut, "Large-eddy lattice-boltzmann modelling of transonic flows," Physics of Fluids **33**, 115112 (2021).

[71]P. Bergé and M. Dubois, "Rayleigh-bénard convection," Contemporary Physics **25**, 535–582 (1984).

[72]N. Ouertatani, N. Ben-Cheikh, B. Beya, and T. Lili, "Numerical simulation of two-dimensional rayleigh–bénard convection in an enclosure," Comptes Rendus Mécanique **336**, 464–470 (2008).

[73]X. He, S. Chen, and R. Zhang, "A lattice boltzmann scheme for incompressible multiphase flow and its application in simulation of rayleigh–taylor instability," Journal of Computational Physics **152**, 642–663 (1999).

[74]D. Chiappini, G. Bella, S. Succi, F. Toschi, and S. Ubertini, "Improved lattice boltzmann without parasitic currents for rayleigh-taylor instability," Communications in Computational Physics **7**, 423 (2010).

[75]S. A. Hosseini, H. Safari, and D. Thevenin, "Lattice boltzmann solver for multiphase flows: Application to high weber and reynolds numbers," Entropy **23**, 166 (2021).

[76]H. Ding, P. D. Spelt, and C. Shu, "Diffuse interface model for incompressible two-phase flows with large density ratios," Journal of Computational Physics **226**, 2078–2095 (2007).

[77]X. He, R. Zhang, S. Chen, and G. D. Doolen, "On the three-dimensional rayleigh–taylor instability," Physics of Fluids **11**, 1143–1152 (1999).

[78]Q. Li, K. Luo, Y. Gao, and Y. He, "Additional interfacial force in lattice boltzmann models for incompressible multiphase flows," Physical Review E **85**, 026704 (2012).

[79]G. Tryggvason, "Numerical simulations of the rayleigh-taylor instability," Journal of Computational Physics **75**, 253–282 (1988).

[80]J.-L. Guermond and L. Quartapelle, "A projection fem for variable density incompressible flows," Journal of Computational Physics **165**, 167–188 (2000).

[81]L. Lee, "A class of high-resolution algorithms for incompressible flows," Computers & fluids **39**, 1022–1032 (2010).

[82]Y. Zu and S. He, "Phase-field-based lattice boltzmann model for incompressible binary fluid systems with density and viscosity contrasts," Physical Review E **87**, 043301 (2013).

[83]B. Morton and J. Middleton, "Scale diagrams for forced plumes," Journal of Fluid Mechanics **58**, 165–176 (1973).

[84]X. Zhou, K. H. Luo, and J. J. Williams, "Study of density effects in turbulent buoyant jets using large-eddy simulation," Theoret. Comput. Fluid Dynamics **15**, 95–120 (2001).

[85]A. Michalke, "Survey on jet instability theory," Progress in Aerospace Sciences **21**, 159–199 (1984).

[86]N. Didden and C.-M. Ho, "Unsteady separation in a boundary layer produced by an impinging jet," Journal of Fluid Mechanics **160**, 235–256 (1985).

[87]S. Menow and M. Rizk, "Large-eddy simulations of forced three-dimensional impinging jets," International journal of computational fluid dynamics **7**, 275–289 (1996).

[88]H. JCR, A. Wray, and P. Moin, "Eddies, streams, and convergence zones in turbulent flows," Studying Turbulence Using Numerical Simulation Databases-I1 , 193 (1988).

[89]A. N. Kolmogorov, "The local structure of turbulence in incompressible viscous fluid for very large reynolds numbers," Cr Acad. Sci. URSS **30**, 301–305 (1941).

[90]N. E. Kotsovinos, "Turbulence spectra in free convection flow," Physics of Fluids A: Fluid Dynamics **3**, 163–167 (1991).

[91]A. Lingens, M. Reeker, and M. Schreiber, "Instability of buoyant diffusion flames," Experiments in Fluids **20**, 241–248 (1996).

[92]B. Gebhart, Y. Jaluria, R. L. Mahajan, and B. Sammakia, "Buoyancy-induced flows and transport," (1988).

[93]C. J. Chen and W. Rodi, "Vertical turbulent buoyant jets: a review of experimental data," Nasa STI/Recon Technical Report A **80**, 23073 (1980).

[94]J. Turner, "Buoyant plumes and thermals," Annual Review of Fluid Mechanics **1**, 29–44 (1969).

[95]B. M. Cetegen, "Behavior of naturally unstable and periodically forced axisymmetric buoyant plumes of helium and helium-air mixtures," Phys. Fluids **9**, 3742–3753 (1997).

[96]K. L. Denman, "Fischer, h. b., e. j. list, r. c. y. koh, j. imberger, and n. a. brooks. 1979. mixing in inland and coastal waters. academic press, inc., new york, xiv + 483 p. $35.00." Limnology and Oceanography **27**, 593–594 (1982).

Appendix A: Expressions for the LBM solver

In regularized LBM, distribution functions will be constructed using an orthogonal polynomial basis. The basis of the D3Q19r lattice used in the current study consists of 19

polynomials, read[17]

$$\mathcal{H}_i^{(0)} \equiv 1 \ , \quad \mathcal{H}_{i,\alpha}^{(1)} \equiv c_{i\alpha} \ , \quad \mathcal{H}_{i,\alpha\beta}^{(2)} \equiv c_{i\alpha}c_{i\beta} - c_s^2\delta_{\alpha\beta}, \tag{A1}$$

$$\mathcal{H}_{i,1}^{(3r)} \equiv \mathcal{H}_{i,xxy}^{(3)} + \mathcal{H}_{i,yzz}^{(3)}, \tag{A2}$$

$$\mathcal{H}_{i,2}^{(3r)} \equiv \mathcal{H}_{i,xzz}^{(3)} + \mathcal{H}_{i,xyy}^{(3)}, \tag{A3}$$

$$\mathcal{H}_{i,3}^{(3r)} \equiv \mathcal{H}_{i,yyz}^{(3)} + \mathcal{H}_{i,xxz}^{(3)}, \tag{A4}$$

$$\mathcal{H}_{i,4}^{(3r)} \equiv \mathcal{H}_{i,xxy}^{(3)} - \mathcal{H}_{i,yzz}^{(3)}, \tag{A5}$$

$$\mathcal{H}_{i,5}^{(3r)} \equiv \mathcal{H}_{i,xzz}^{(3)} - \mathcal{H}_{i,xyy}^{(3)}, \tag{A6}$$

$$\mathcal{H}_{i,6}^{(3r)} \equiv \mathcal{H}_{i,yyz}^{(3)} - \mathcal{H}_{i,xxz}^{(3)}, \tag{A7}$$

$$\mathcal{H}_{i,1}^{(4r)} \equiv \frac{4}{9}\left(3+2\sqrt{3}\right)\mathcal{D}_{i,xyz}^{(4)} + \frac{4}{9}\left(3-\sqrt{3}\right)\mathcal{D}_{i,xzy}^{(4)} + \frac{4}{9}\left(3-\sqrt{3}\right)\mathcal{D}_{i,zyx}^{(4)}, \tag{A8}$$

$$\mathcal{H}_{i,2}^{(4r)} \equiv \frac{4}{9}\left(3+2\sqrt{3}\right)\mathcal{D}_{i,xzy}^{(4)} + \frac{4}{9}\left(3-\sqrt{3}\right)\mathcal{D}_{i,xyz}^{(4)} + \frac{4}{9}\left(3-\sqrt{3}\right)\mathcal{D}_{i,zyx}^{(4)}, \tag{A9}$$

$$\mathcal{H}_{i,3}^{(4r)} \equiv \frac{4}{9}\left(3+2\sqrt{3}\right)\mathcal{D}_{i,zyx}^{(4)} + \frac{4}{9}\left(3-\sqrt{3}\right)\mathcal{D}_{i,xzy}^{(4)} + \frac{4}{9}\left(3-\sqrt{3}\right)\mathcal{D}_{i,xyz}^{(4)}, \tag{A10}$$

where

$$\mathcal{H}_{i,\alpha\beta\gamma}^{(3)} \equiv c_{i\alpha}c_{i\beta}c_{i\gamma} - c_s^2[c_{i\alpha}\delta_{\beta\gamma} + c_{i\beta}\delta_{\gamma\alpha} + c_{i\gamma}\delta_{\alpha\beta}] \ , \tag{A11}$$

$$\mathcal{D}_{i,\alpha\beta\gamma}^{(4)} \equiv \mathcal{H}_{i,\alpha\alpha\beta\beta}^{(4)} + \frac{c_s^2}{2}\mathcal{H}_{i,\gamma\gamma}^{(2)} \ , \tag{A12}$$

$$\begin{aligned}\mathcal{H}_{i,\alpha\beta\gamma\delta}^{(4)} \equiv & c_{i\alpha}c_{i\beta}c_{i\gamma}c_{i\delta} + c_s^4(\delta_{\alpha\beta}\delta_{\gamma\delta} + \delta_{\beta\gamma}\delta_{\delta\alpha} + \delta_{\delta\alpha}\delta_{\beta\gamma}) \\ & - c_s^2(c_{i\alpha}c_{i\beta}\delta_{\gamma\delta} + c_{i\beta}c_{i\gamma}\delta_{\delta\alpha} + c_{i\gamma}c_{i\delta}\delta_{\alpha\beta} + c_{i\delta}c_{i\alpha}\delta_{\beta\gamma} + c_{i\gamma}c_{i\alpha}\delta_{\beta\delta} + c_{i\beta}c_{i\delta}\delta_{\alpha\gamma}) \, .\end{aligned} \tag{A13}$$

693 Any distribution function in the D3Q19r lattice can be written as a (weighted) sum of
694 the contributions from each base polynomial. For instance, the equilibrium distribution in
695 equation (14) reads

$$f_i^{\mathrm{eq},19r} = \omega_i \left\{ a^{(0),\mathrm{eq}} + \frac{\mathcal{H}_{i,\alpha}^{(1)}}{c_s^2}a_\alpha^{(1),\mathrm{eq}} + \frac{\mathcal{H}_{i,\alpha\beta}^{(2)}}{2c_s^4}a_{\alpha\beta}^{(2),\mathrm{eq}} + \frac{\mathcal{H}_{i,\gamma}^{(3r)}}{6c_s^6}a_\gamma^{(3r),\mathrm{eq}} + \frac{\mathcal{H}_{i,\delta}^{(4r)}}{24c_s^8}a_\delta^{(4r),\mathrm{eq}} \right\} \ , \tag{A14}$$

where

$$a^{(0),\mathrm{eq}} = \rho\theta \ , \quad a^{(1),\mathrm{eq}}_{\alpha} = \rho u_{\alpha} \ , \quad a^{(2),\mathrm{eq}}_{\alpha\beta} = \rho u_{\alpha} u_{\beta} \tag{A15}$$

$$a^{(3r),\mathrm{eq}}_{1} = 3(\rho u_x u_x u_y + \rho u_y u_z u_z) \ , \tag{A16}$$

$$a^{(3r),\mathrm{eq}}_{2} = 3(\rho u_x u_z u_z + \rho u_x u_y u_y) \ , \tag{A17}$$

$$a^{(3r),\mathrm{eq}}_{3} = 3(\rho u_y u_y u_z + \rho u_x u_x u_z) \ , \tag{A18}$$

$$a^{(3r),\mathrm{eq}}_{4} = \rho u_x u_x u_y - \rho u_y u_z u_z \ , \tag{A19}$$

$$a^{(3r),\mathrm{eq}}_{5} = \rho u_x u_z u_z - \rho u_x u_y u_y \ , \tag{A20}$$

$$a^{(3r),\mathrm{eq}}_{6} = \rho u_y u_y u_z - \rho u_x u_x u_z \ , \tag{A21}$$

$$a^{(4r),\mathrm{eq}}_{1} = -\rho c_s^2 \left[\frac{-4\sqrt{3}-6}{9} u_z^2 + \frac{2\sqrt{3}-6}{9} \left(u_x^2 + u_y^2 \right) \right] , \tag{A22}$$

$$a^{(4r),\mathrm{eq}}_{2} = -\rho c_s^2 \left[\frac{-4\sqrt{3}-6}{9} u_y^2 + \frac{2\sqrt{3}-6}{9} \left(u_x^2 + u_z^2 \right) \right] , \tag{A23}$$

$$a^{(4r),\mathrm{eq}}_{3} = -\rho c_s^2 \left[\frac{-4\sqrt{3}-6}{9} u_x^2 + \frac{2\sqrt{3}-6}{9} \left(u_y^2 + u_z^2 \right) \right] . \tag{A24}$$

It is worth noting that the the forth-order coefficients ($a^{(4),\mathrm{eq}}$) are added to improve the isotropicity of the lattice, which could be quite important considering the round jet simulation in the current study.

The third-order off-equilibrium terms are reconstructed recursively from the second-order non-equilibrium tensor as

$$\begin{aligned}
a^{(3),\mathrm{neq}}_{\alpha\beta\gamma} &= u_{\alpha} a^{(2),\mathrm{neq}}_{\beta\gamma} + u_{\beta} a^{(2),\mathrm{neq}}_{\alpha\gamma} + u_{\gamma} a^{(2),\mathrm{neq}}_{\alpha\beta} \\
a^{(3r),\mathrm{neq}}_{1} &\equiv a^{(3),\mathrm{neq}}_{xxy} + a^{(3),\mathrm{neq}}_{yzz} \\
a^{(3r),\mathrm{neq}}_{2} &\equiv a^{(3),\mathrm{neq}}_{xzz} + a^{(3),\mathrm{neq}}_{xyy} \\
a^{(3r),\mathrm{neq}}_{3} &\equiv a^{(3),\mathrm{neq}}_{yyz} + a^{(3),\mathrm{neq}}_{xxz} \\
a^{(3r),\mathrm{neq}}_{4} &\equiv a^{(3),\mathrm{neq}}_{xxy} - a^{(3),\mathrm{neq}}_{yzz} \\
a^{(3r),\mathrm{neq}}_{5} &\equiv a^{(3),\mathrm{neq}}_{xzz} - a^{(3),\mathrm{neq}}_{xyy} \\
a^{(3r),\mathrm{neq}}_{6} &\equiv a^{(3),\mathrm{neq}}_{yyz} - a^{(3),\mathrm{neq}}_{xxz}
\end{aligned} \tag{A25}$$

Depending on the order of the Gauss-Hermite quadrature[67] used in the LB model, an adequate forcing term should be added to achieve a correct viscous stress tensor:

$$a^{\mathrm{neq}}_{\alpha\beta} \approx -\Pi_{\alpha\beta} = -\mu(\frac{\partial u_{\alpha}}{\partial x_{\beta}} + \frac{\partial u_{\beta}}{\partial x_{\alpha}} - \frac{2}{D}\frac{\partial u_{\gamma}}{\partial x_{\gamma}}\delta_{\alpha\beta}), \tag{A26}$$

with D the spatial dimension. For the D3Q19r basis, the projected forcing term reads as

$$a_{\alpha\beta}^{F^E} = c_s^2 u_\alpha \left[\frac{\partial(\rho(1-\theta))}{\partial x_\beta}\right] + c_s^2 u_\beta \left[\frac{\partial(\rho(1-\theta))}{\partial x_\alpha}\right] + \delta_{\alpha\beta}\rho c_s^2 \frac{2}{D}\frac{\partial u_\gamma}{\partial x_\gamma} - a_{\alpha\beta}^{\text{cor}} + a_{\alpha\beta}^{F_D} \quad \text{(A27)}$$

where $a_{\alpha\beta}^{\text{cor}}$ is a correction tensor due to the deflection of second order moments of the population introduced by the modification of the mass equation, which can be evaluated as

$$a_{\alpha\beta}^{\text{cor}} \equiv c_s^2 \delta_{\alpha\beta} \frac{\partial(\rho(1-\theta))}{\partial t}, \quad \text{(A28)}$$

which can be discretized using a backward Euler operator and $a_{\alpha\beta}^{F_D}$ the correction tensor due to the defect of the lattice at third order

$$a_{\alpha\beta}^{F_D} = -\begin{pmatrix} (\rho u_x^3)_{,x} & (\rho u_x u_y u_z)_{,z} & (\rho u_x u_y u_z)_{,y} \\ (\rho u_x u_y u_z)_{,z} & (\rho u_y^3)_{,y} & (\rho u_x u_y u_z)_{,x} \\ (\rho u_x u_y u_z)_{,y} & (\rho u_x u_y u_z)_{,x} & (\rho u_z^3)_{,z} \end{pmatrix} \quad \text{(A29)}$$

where all the differential operations are performed using first order upwind FD except for the divergence operator for which a second order centered FD scheme was employed. The final expression of the forcing term is then

$$F_i^E = \frac{\omega_i}{2c_s^4} \mathcal{H}_{i,\alpha\beta}^{(2)} a_{\alpha\beta}^{F^E} + F_i^g, \quad \text{(A30)}$$

where F_i^g is the gravity force term defined as

$$F_i^g = \omega_i \left[\frac{\rho g_\alpha \mathcal{H}_{i,\alpha}^{(1)}}{c_s^2} + \frac{(\rho u_\alpha g_\beta + \rho u_\beta g_\alpha)\mathcal{H}_{i,\alpha\beta}^{(2)}}{2c_s^4}\right], \quad \text{(A31)}$$

where g_α is the gravity acceleration in the direction α.